J. Fluid Mech. (2023), *vol*. 959, A37, doi:10.1017/jfm.2023.161

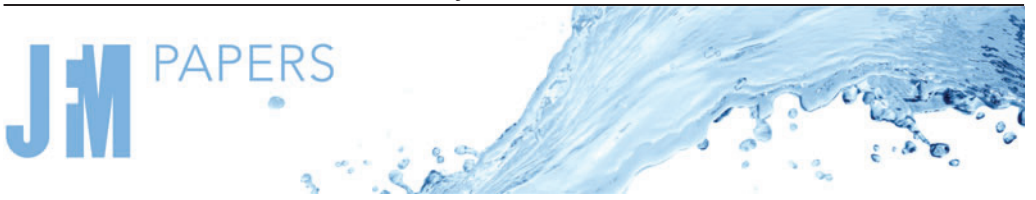

Divergent Richtmyer–Meshkov instability on a heavy gas layer

Duo Zhang[1], **Juchun Ding**[1,†], **Ting Si**[1] **and Xisheng Luo**[1,†]

[1]Advanced Propulsion Laboratory, Department of Modern Mechanics, University of Science and Technology of China, Hefei 230026, PR China

(Received 22 August 2022; revised 7 February 2023; accepted 21 February 2023)

Experiments on divergent Richtmyer–Meshkov (RM) instability at a heavy gas layer are performed in a specially designed shock tube. A novel soap-film technique is extended to generate gas layers with controllable thicknesses and shapes. An unperturbed gas layer is first examined and its two interfaces are found to move uniformly at the early stage and be decelerated later. A general one-dimensional theory applicable to an arbitrary-thickness layer is established, which gives a good prediction of the layer motion in divergent geometry. Then, six kinds of perturbed SF_6 layers with various thicknesses and shapes surrounded by air are examined. At the early stage, the amplitude growths of the inner interface for various-thickness layers collapse quite well and also can be predicted by the Bell model for cylindrical RM instability at a single interface, which indicates a negligible interface coupling effect. Later, a rarefaction wave accelerates the inner interface, causing a dramatic rise in the growth rate. It is found that a thicker gas layer will result in a larger extent that the rarefaction wave can promote the instability growth. A modified Bell model accounting for both Rayleigh–Taylor (RT) instability and interface stretching caused by a rarefaction wave is established, which well reproduces the quick instability growth. At late stages, reverberating waves inside the layer are negligibly weak such that the inner interface growth is dominated by RM instability and RT stability. The major factors driving the outer interface development are a compression wave and interface coupling. A new interface coupling phenomenon existing uniquely in divergent geometry caused by the gradual thinning of the gas layer is observed and also modelled.

Key words: shock waves, shear-flow instability

1. Introduction

The growth of perturbations at an interface between two fluids of different property, driven by an external force or an acceleration field, is generally referred to as the

† Email addresses for correspondence: djc@ustc.edu.cn; xluo@ustc.edu.cn

Rayleigh–Taylor (RT) instability (Rayleigh 1883; Taylor 1950). A similar hydrodynamic instability is the Richtmyer–Meshkov (RM) instability (Richtmyer 1960; Meshkov 1969), which occurs when a perturbed interface is subjected to an impulsive force typically by a shock wave. Although RM and RT instabilities share common evolution processes such as the formation of bubbles (a light fluid rises into a heavy one) and spikes (a heavy fluid falls freely into a light one), their perturbation growth rates are distinctly different. Specifically, RT perturbation grows exponentially with time at the early stage and later at a constant asymptotic growth rate, whereas RM perturbation grows linearly at the early stage and later nonlinearly at a time-decaying growth rate. Over the past decades, RM instability has attracted widespread attention due to its significance in academic research, e.g. compressible turbulence (Mohaghar *et al.* 2019; Groom & Thornber 2021) and vortex dynamics (Peng *et al.* 2021), as well as the important role in industrial fields such as inertial confinement fusion (ICF) (Betti & Hurricane 2016).

In terms of the flow cross-section area, RM instability can be categorized into two types: area-invariant RM instability and area-varied RM instability. The former usually refers to planar shock-induced RM instability, which has been extensively studied by experimentalists (Biamino *et al.* 2015; Reese *et al.* 2018; Liang *et al.* 2021; Sewell *et al.* 2021), theorists (Richtmyer 1960; Zhang & Sohn 1997; Dimonte & Ramaprabhu 2010; Zhang & Guo 2016) and numerical experts (Schilling & Latini 2010; Lombardini, Pullin & Meiron 2014; Wonga & Lelea 2017; Li *et al.* 2022). It is widely accepted that pressure disturbance (caused by pressure waves behind the refracted shock) and baroclinic vorticity (caused by the misalignment of pressure and density gradients) are the major mechanisms for the growth of area-invariant RM instability (Brouillette 2002; Ranjan, Oakley & Bonazza 2011; Zhou 2017). Two typical representatives of area-varied RM instability are convergent shock-induced RM instability (i.e. convergent RM instability) (Vandenboomgaerde *et al.* 2018) and divergent shock-induced RM instability (i.e. divergent RM instability) (Li *et al.* 2020). In addition to the flow mechanisms of area-invariant RM instability, the area-varied counterpart involves new physical regimes such as geometric contraction/expansion (Penney & Price 1945; Bell 1951; Plesset 1954; Epstein 2004) and RT stability/instability caused by flow deceleration (Ding *et al.* 2017*b*; Luo *et al.* 2018), and thus presents more possibilities and complexities for the instability growth.

Convergent RM instability, which involves an initial setting more relevant to hydrodynamic instabilities in ICF, has become increasingly more attractive in recent years. The first experiments on convergent RM instability were carried out by Hosseini, Ogawa & Takayama (2000) in a vertical coaxial shock tube. This coaxial shock tube was later improved by Si *et al.* (2015) and Lei *et al.* (2017), in which the development of convergent RM instability at a polygonal/single-mode interface was obtained with a high-speed imaging technique. Also, Dimotakis & Samtaney (2006) proposed a gas-lens technique, with which cylindrically/spherically convergent shocks can be generated through shock refraction (Biamino *et al.* 2015; Vandenboomgaerde *et al.* 2018). Based on shock dynamics theory, a horizontal shock tube with a special wall profile that smoothly transforms an initial planar shock into a cylindrical one was designed by Zhai *et al.* (2010). Recently, clear observation of convergent RM instability was achieved (Ding *et al.* 2017*b*, 2019; Li *et al.* 2020) in a novel semi-annular shock tube, and the influences of geometric contraction/expansion and RT instability/stability on the perturbation growth were quantified.

The development of convergent RM instability usually involves two stages: a convergent stage (i.e. instability growth after an incident convergent shock strikes the interface) and

a divergent stage (i.e. instability growth after a divergent shock that is reflected from the geometric centre impacts the deforming interface). Previous studies on convergent RM instability were mainly focused on the convergent stage (Ding *et al.* 2017*a*; Vandenboomgaerde *et al.* 2018; Ding *et al.* 2019) and little attention was paid to the divergent stage. The main reasons are given below. First, the interface has been severely distorted before the arrival of the divergent shock. Thus, it is very difficult to accurately characterize the interface shape. Second, the pre-reshock flow field exhibits strong non-uniformity along both radial and circumferential directions, which greatly impedes the flow analysis. It is therefore highly desirable to conduct an experimental study on divergent RM instability with controllable initial conditions, which is essential for understanding the flow regimes at the divergent stage of convergent RM instability. In addition, divergent RM instability is a good approximation of hydrodynamic instability in supernova explosion (Arnett *et al.* 1989; Kuranz *et al.* 2018), where stellar collapse produces a spherically divergent shock that passes across multi-layer elements, and thus the relevant study is helpful for explaining the formation of supernova remnant (Miles *et al.* 2004; Ribeyre, Tikhonchuk & Bouquet 2004; Musci *et al.* 2020). Moreover, as another typical representative of area-varied RM instability, study on divergent RM instability would complete the fundamental understanding of area-varied RM instability.

A key issue for the experimental study of divergent RM instability is to generate a stable, controllable, repeatable divergent shock wave. Based on shock dynamics theory, Li *et al.* (2020) recently designed a novel divergent shock tube, in which ideal cylindrical divergent shocks can be generated. The first shock-tube experiments on divergent RM instability in this facility showed that the growth of divergent RM instability is much slower than the planar and convergent counterparts, and also nonlinearity is far weaker. Nevertheless, the fundamental configuration (a cylindrical shock impacts a single-mode interface) considered by Li *et al.* (2020) is too simple to represent the instability in practical applications such as ICF, where the instability occurs simultaneously on multiple interfaces (the ICF target is usually composed of an outer ablator, middle deuterium–tritium ice and inner deuterium–tritium gas). Recent studies on RM instability at two interfaces in planar and convergent geometries showed that there are complex waves reverberating between the two interfaces, which cause RT stability/instability (Henry de Frahan, Movahed & Johnsen 2014; Liang *et al.* 2020; Sun *et al.* 2020; Liang & Luo 2021*a*, 2022). Particularly, in convergent geometry, two interfaces with various initial radii could present different radial trajectories, and consequently geometric expansion and the RT effect may behave differently (Ding *et al.* 2019). Moreover, for two adjacent interfaces, the interface coupling effect becomes evident (Jacobs *et al.* 1995; Mikaelian 1995; Liang *et al.* 2020), which considerably affects the instability development at each interface. To the best of the authors' knowledge, there is no published work on divergent RM instability at multiple interfaces. In divergent geometry, the motions of interfaces and waves as well as the interface coupling strength are distinctly different from the convergent and planar counterparts, which would significantly affect the instability growth. This motivates the present study.

In this work, we shall perform an experimental study on divergent RM instability at an SF_6 gas layer surrounded by air. Three kinds of unperturbed SF_6 layers with various thicknesses are first examined. By considering the influences of reverberating waves inside the layer and pressure non-uniformity along the radial direction, a one-dimensional (1-D) theory is established, which well describes the layer motion. Then, six types of perturbed layers with various thicknesses, amplitudes and wavelengths of the inner interface are examined. The influences of interface coupling and initial interface perturbation on the

instability growth are analysed in detail. Finally, modified models accounting for the wave influence and RT instability/stability are proposed to predict the instability growth at the inner and outer interfaces of the layer.

2. Experimental methods

The experiments are carried out in a divergent shock tube that is designed based on shock dynamics theory. A sketch of the curved part of the shock tube creating the planar-convergent–planar-divergent shock transformations is shown in figure 1(*a*) (not drawn to scale). The curved part has a designed length of 2100.0 mm (the whole shock tube is 6400.0 mm long) and an inner height of 7.0 mm, and its left-hand end is connected to the driven section. In experiment, a planar shock wave of Mach number (*Ma*) of 1.35 is first generated after the rupture of the diaphragm between the driver and driven sections. When this planar shock propagates along the concave wall *AB*, it is gradually transformed to a cylindrical convergent shock. As time proceeds, the cylindrical shock converges along the oblique wall *BC* with its strength being gradually enhanced. Later, it is converted back into a planar one by the convex wall *CD*. This planar shock has an *Ma* of 1.71, which is stronger than the incident planar shock (Zhan *et al.* 2018). Finally, the planar shock is converted to a cylindrical divergent shock by the convex wall *EF*. Afterwards, the divergent shock propagates outwards and subsequently collides with the downstream SF_6 gas layer, triggering the divergent RM instability. The design principle of the curved walls (*AB* and *CD*) executing the planar-converging–planar shock transformation has been detailed and also fully validated in previous works (Zhai *et al.* 2010; Zhan *et al.* 2018). In this work, we generalize the same principle to the design of the convex wall *EF* for the planar-divergent shock transformation. For more details, readers are referred to the recent work of Li *et al.* (2020). A divergent shock releases energy and its strength becomes increasingly weaker with time. To ensure the successful generation of a divergent shock, the initial planar shock should be relatively strong. An advantage of the present design is to intensify the initial planar shock, which is essential for producing the divergent shock. Specifically, compared to a rectangular cross-section with the same inner dimension as the throat of the present shock tube, the present design enables the generation of a stronger planar shock under the same pressure ratio between the driver and driven sections. This could greatly reduce the experimental difficulty for generating strong shocks and also extend the shock strength range under the available experimental conditions.

A novel soap-film technique, which was recently developed for generating well-defined single interfaces in a divergent shock tube (Li *et al.* 2020), is extended to generate gas layers with controllable shapes in this work. As illustrated in figure 1(*c*), the gas layer is formed in a device composed of sections I, II and III. These three sections are made up of transparent acrylic plates (3 mm thick) sculpted by a high-precision engraving machine and the shape of the whole device is precisely controlled so as to match with the divergent test section. Due to the surface tension of soap film, it is difficult to generate a soap film with a desired shape without any constraints or supports. This is the reason why spherical soap bubbles can only be seen in nature. Fortunately, previous studies have found that thin filaments can be used to constrain the soap film, changing its shape, and meanwhile they produce a negligible influence on the flow (Liu *et al.* 2018; Li *et al.* 2020; Liang & Luo 2021*b*). This provides a novel way to generate soap-film interfaces with desired shapes. In this work, we use such a method to generate gas layers with two controllable surfaces. Specifically, four grooves (0.75 mm thick and 0.5 mm wide) that present the same shapes as the boundaries of the desired gas layer are engraved on the internal surfaces of the upper and lower plates. Then, four thin filaments (1.0 mm thick and 0.5 mm wide)

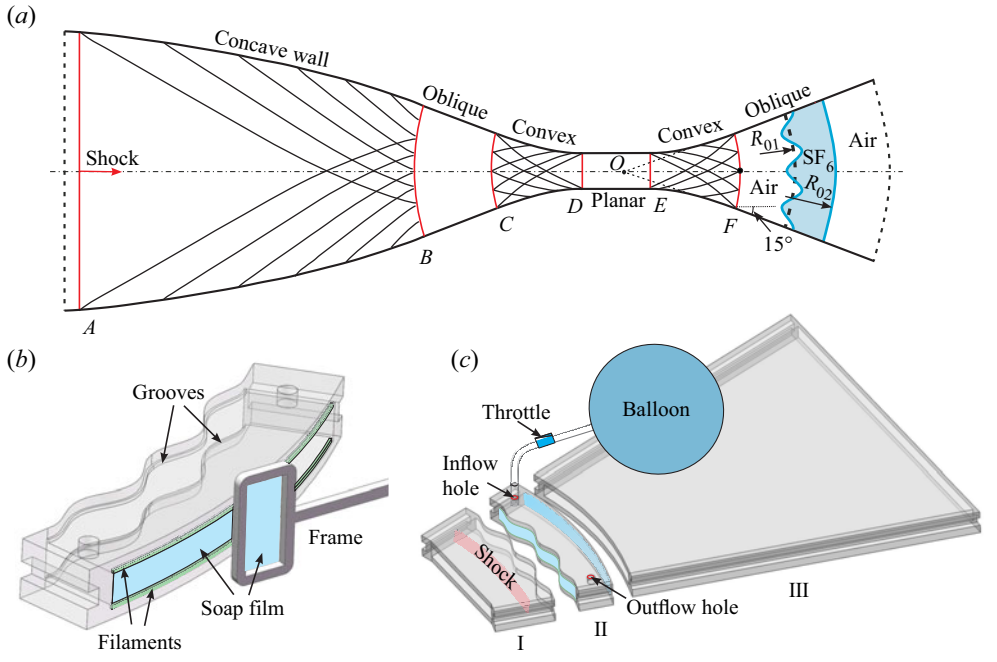

Figure 1. (*a*) Sketch of the curved part of the divergent shock tube, (*b*) an enlarged view of section II of the interface-formation device and (*c*) a drawing of the interface-formation device.

with the same shapes as the grooves are respectively inserted into the four grooves to produce the required constraints. The height of the filaments protruding into the flow field is less than 0.3 mm and thus produces a negligible influence on the flow field. As a rectangular frame dipped with soap solution (60 % distilled water, 20 % sodium oleate and 20 % glycerin) is pulled along the upper and lower filaments on each side of section II, a gas layer with two soap-film interfaces is immediately formed. Subsequently, sections I, II and III are successively inserted into a predesigned drawer. Then, SF_6 gas in a balloon is pumped into section II through an inflow hole, and meanwhile air is exhausted through an outflow hole. To ensure a high concentration of SF_6 inside the layer, an oxygen concentration detector is placed at the outflow hole to monitor the exhausted gas in real time. When the oxygen concentration measured reaches the experimental requirement (below 2 %), the drawer containing sections I, II and III is quickly inserted into the test section and subsequently the experiment is conducted. Note the initial conditions of the present experiments including the shock Mach number, the gas layer shape and the gas concentration can be well controlled, which ensures the high repeatability of experimental results. Hence, the data for each case presented hereinafter are from one experimental run.

In this work, the gas layer interface at a smaller radius is defined as the inner interface, and the other one as the outer interface. In a cylindrical coordinate system, the inner interface can be parametrized as $r_1(\theta) = R_{01} + a_{01}\cos(n\theta + \pi)$. Here, R_{01} stands for the initial radius of the inner interface ($R_{01} = 150$ mm in this work), n for the azimuthal mode number ($n = 24$ or 36 is adopted for adapting to the test section), θ for the azimuthal angle and a_{01} for the initial amplitude of the inner interface. The undisturbed outer interface is described as $r_2(\theta) = R_{02}$ with R_{02} being the initial radius of the outer interface. The flow field is recorded by a high-speed schlieren system that is composed of a high-speed video camera (FASTCAM SA5, Photron Limited), a DC stabilized light source

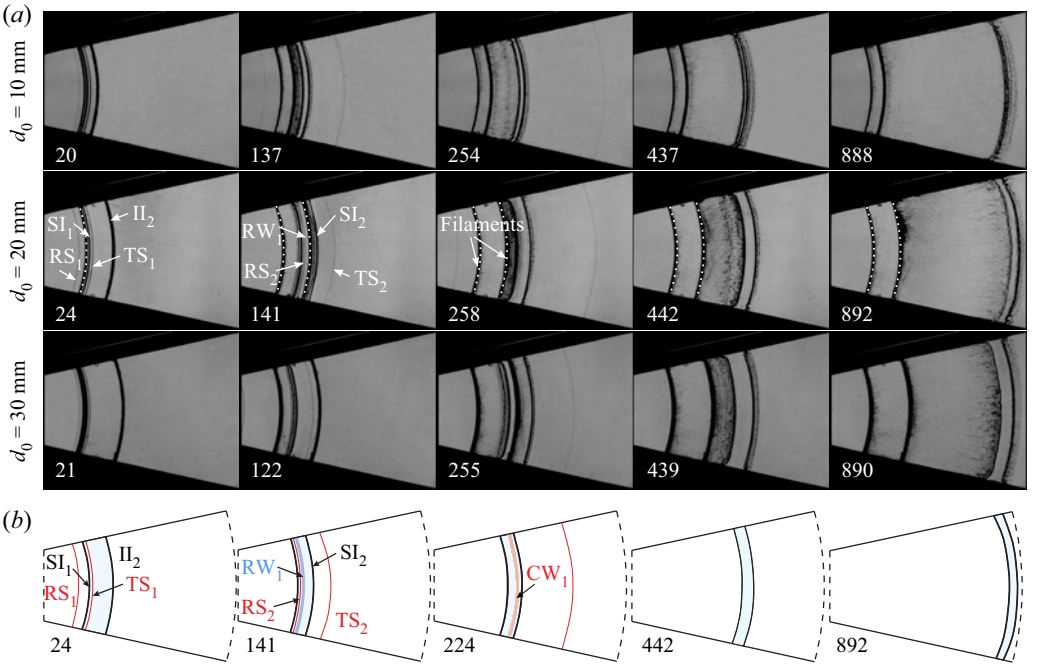

Figure 2. (*a*) Sequences of schlieren images showing the movements of the unperturbed gas layers of different thickness (d_0) after the impact of a cylindrically divergent shock and (*b*) sketches of the wave patterns and interface morphologies at typical moments for the $d_0 = 20$ mm layer. The lines left behind at the initial interface locations in panel (*a*), which are marked by white dot lines, indicate the protruding filaments. Here, II_2 is the initial outer interface; SI_1, the shocked inner interface; SI_2, the shocked outer interface; TS_j, jth transmitted shock; RS_j, jth reflected shock; RW_1, the rarefaction wave reflected from the outer interface; and CW_1, the compression wave reflected from the inner interface. The unit of numbers is μs.

(DCR III, SCHOTT North America, Inc.) and multiple optical lens groups. The frame rate of the high-speed camera is set to be 50 000 f.p.s. with a shutter time of 1 μs. The spatial resolution of the schlieren images obtained is 0.38 mm pixel^{-1}. The ambient pressure and temperature are approximately 101.3 kPa and 301.0 K, respectively.

3. Results and discussions

3.1. *Quasi-1-D experimental results and analysis*

Quasi-1-D experiments corresponding to an undisturbed cylindrical SF_6 layer surrounded by air impacted by a cylindrically divergent shock are first considered. Sequences of schlieren images illustrating the movements of undisturbed SF_6 layers with different thicknesses (d_0) are displayed in figure 2(*a*). Here, we take the $d_0 = 20$ mm case as an example to detail the motions of waves and interfaces. At the beginning, an incident cylindrical shock (ICS) expands outwards and then impinges upon the inner interface (II_1) of the layer, bifurcating into an inward-moving reflected shock (RS_1) and an outward-moving transmitted shock (TS_1). After that, the shocked inner interface (SI_1) starts moving and gradually leaves its original position. Meanwhile, the shock impact causes the soap film to atomize into small droplets, resulting in the thickening of SI_1 in the schlieren images (258 μs). The relationship between the size of the atomized soap droplets and the incident shock strength has been investigated by Cohen (1991) and Ranjan *et al.* (2008). According to their work, the mean radius of the soap droplets

in the present experiment is estimated to be approximately 30 μm for the shock wave of $Ma \sim 1.3$. Previous studies on RM instability adopting such a soap-film technique (Ding *et al.* 2017*a*; Liu *et al.* 2018) showed that the experimental results are in good agreement with the numerical simulations and theoretical predictions, which indicates a negligible influence of the soap droplets on the interface evolution. Later, the outgoing TS_1 collides with the initial outer interface (II_2) of the layer, splitting into a second transmitted shock (TS_2) and an inward-moving rarefaction wave (RW_1). During this process, a weak reflected shock (RS_2) is produced, which is caused by the interaction of TS_1 with the protruding filaments. This reflected shock has also been observed in previous experiments (Vandenboomgaerde *et al.* 2018; Liang *et al.* 2020) and its influence on the instability development was demonstrated to be negligible due to the weak strength. Later, RW_1 stretches and accelerates the shocked inner interface SI_1. At the same time, an outward-moving compression wave (CW_1) is generated inside the layer (not visible in schlieren images due to the weak intensity). Afterwards, CW_1 compresses and accelerates the shocked outer interface SI_2, generating a second rarefaction wave (RW_2), which later interacts with SI_1 again. The above wave propagation process would be repeated many times inside the layer until the waves are negligibly weak. In this work, after CW_1 passes across SI_2, the waves reverberating inside the gas layer are very weak and can be ignored. The lines left behind at the initial interface locations in figure 2(*a*) indicate the protruding filaments, which are marked by white dotted lines. Sketches of the waves and interfaces at typical moments for the $d_0 = 20$ mm case are given in figure 2(*b*). Differing from the layer motion in planar and convergent geometries, the gas layer in divergent geometry becomes increasingly thinner with time. Particularly, the inner and outer interfaces coalesce to one at 888 μs for the $d_0 = 10$ mm case. The time origin in this work is defined as the moment at which the incident shock arrives at the mean position of the inner interface.

Although a gas concentration detector is adopted to measure the oxygen concentration of the gas mixture exhausted from the outflow hole, it can only ensure a high concentration of SF_6 inside the layer rather than directly measuring the mass fraction of SF_6. In this work, we estimate the mass fraction of SF_6 inside the layer using the following method. For a planar shock impacting a flat light/heavy interface, the subsequent flow is composed of four uniform regions separated by a reflected shock, a transmitted shock and the interface. According to 1-D gas dynamics theory, we can establish relations for the flow parameters on both sides of the reflected and transmitted shocks. With the compatibility relation at the interface (i.e. velocity and pressure continuity), the following equation can be derived:

$$\left[\frac{(\Lambda_2-1)\,\rho_1}{(\Lambda_1-1)\,\rho_2}\right]^{1/2}\frac{P_t-1}{(P_t\Lambda_2+1)^{1/2}}=\frac{P_i-1}{(P_i\Lambda_1+1)^{1/2}}-\left(\frac{\rho_1}{\rho_1'}\right)^{1/2}\frac{P_t-P_i}{(P_t\Lambda_1+P_i)^{1/2}},\quad(3.1)$$

where

$$\left.\begin{aligned}\Lambda_1&=(\gamma_1+1)/(\gamma_1-1),\\ \Lambda_2&=(\gamma_2+1)/(\gamma_2-1),\\ P_i&=1+2\gamma_1/(\gamma_1+1)\left(M_i^2-1\right),\\ \rho_1/\rho_1'&=[(\gamma_1-1)M_i^2+2]/[(\gamma_1+1)M_i^2].\end{aligned}\right\}\quad(3.2)$$

Here, γ_1 (γ_2) and ρ_1 (ρ_2) refer to the specific heat ratio and the fluid density outside (inside) the layer, respectively, P_i (P_t) to the pressure ratio across the incident shock (transmitted shock), ρ_1' to the fluid density behind the incident shock, and M_i to the Mach number of the incident shock. In experiment, the gas outside the layer is pure air. The incident shock has a

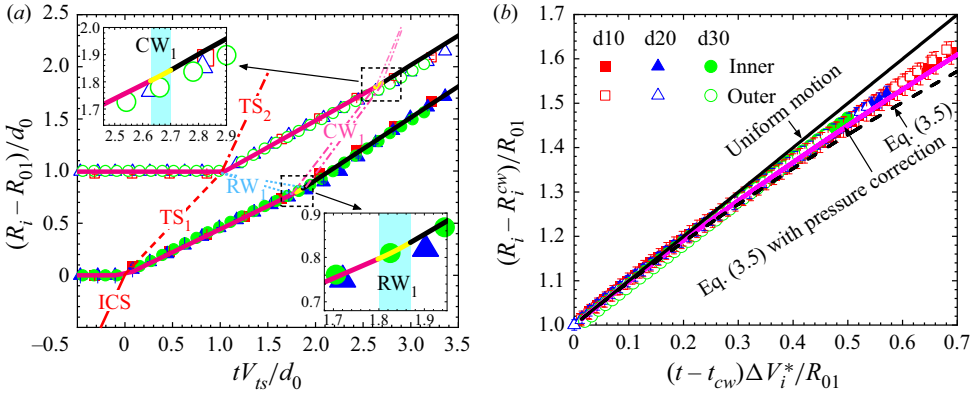

Figure 3. Trajectories of the inner and outer interfaces at (*a*) early and (*b*) late stages for unperturbed gas layers with different thicknesses ($d_0 = 10$ mm, 20 mm, 30 mm). A wave diagram is also included in panel (*a*). The solid line in panel (*a*) refers to the prediction of 1-D theory of Liang & Luo (2021*a*). ICS, incident cylindrical shock. The other symbols are the same as those in figure 2.

measured speed of 432.7 m s^{-1} before its collision with the inner interface, corresponding to $M_i = 1.26$. The value of mass fraction is obtained by the iterative method via numerical calculation. Specifically, giving an arbitrary initial value between 0 and 1 for the mass fraction of SF_6 inside the layer, the flow parameters inside the layer (e.g. ρ_2 and γ_2) can be obtained. Substituting the known parameters into (3.1), the pressure ratio across the transmitted shock (P_t) can be solved and then the strength of the transmitted shock is available. If the calculated strength of the transmitted shock is stronger than the measured one, the value of mass fraction is reduced; otherwise, it is increased. This process is repeated many times until the calculated value is in good agreement with the measured one (i.e. their difference is lower than 0.1 %). For the unperturbed case here, the mass fraction of SF_6 inside the layer is calculated to be 95.0 %. With this value, the flow velocity behind TS_1 is calculated to be 92.5 m s^{-1} based on gas dynamics theory, which agrees reasonably with the experimental measurement (96.7 $\pm$ 1.4 m s^{-1}). This demonstrates good reliability of the present calculation method. Also, it indicates a negligible influence of soap droplets on the flow. The inner and outer interface maintain a nearly cylindrical shape during the experimental time, which indicates a limited influence of the boundary layer on the interface movement.

Dimensionless variations of the displacements of the inner and outer interfaces with time for all gas layers are plotted in figure 3. It is seen that both inner and outer interfaces move uniformly at the early stage (before CW_1 crosses the outer interface, figure 3*a*), but decelerate continuously at the late stage (figure 3*b*). For the early-stage motion, time is scaled as tV_{ts}/d_0 with V_{ts} being the initial speed of TS_1 and the interface displacement as $(R_i - R_{01})/d_0$ with R_i being the average radius of interface i ($i = 1$ for inner interface and $i = 2$ for outer interface). For the late-stage deceleration motion (figure 3*b*), time is scaled as $(t - t_{cw})\Delta V_i^*/R_{01}$ with t_{cw} being the moment at which CW_1 encounters the outer interface and ΔV_1^* (ΔV_2^*) being the inner (outer) interface velocity after the impact of RW_1 (CW_1). The interface displacement is scaled as $(R_i - R_i^{cw})/R_{01}$ with R_i^{cw} being the radius of interface i at t_{cw}. Using the above normalization, the dimensionless displacements of the inner (outer) interfaces of various-thickness layers converge at all stages. It indicates that we can establish a general 1-D theory applicable to an arbitrary-thickness layer to describe the motion of a shocked gas layer in divergent geometry. Note that the interface

thickness in schlieren images introduces the measurement uncertainty. At the early stage, the interface occupies approximately three pixels, corresponding to the error bar of 1.1 mm. Later, the interface becomes gradually thicker due to the influences of gas diffusion and soap droplets, corresponding to the error bar of 2.3 mm. These error bars are smaller than the size of the symbols in figure 3(*a*), and thus not visible.

We first consider the layer motion at the early stage. After the shock impact, the inner interface SI_1 moves at a constant velocity of 0.47, corresponding to a dimensional velocity of $\Delta V_1 = 96.7\,\mathrm{m\,s^{-1}}$. Later, RW_1 accelerates the inner interface, and its dimensionless velocity increases to 0.60 (corresponding to $\Delta V_1^* = 125.1\,\mathrm{m\,s^{-1}}$). After the impact of TS_1, the outer interface SI_2 speeds up quickly to 0.54 (corresponding to $\Delta V_2 = 111.4\,\mathrm{m\,s^{-1}}$) and later is further accelerated to 0.58 by CW_1 (corresponding to $\Delta V_2^* = 119.5\,\mathrm{m\,s^{-1}}$). The present result indicates that the interface movement at the early stage is mainly affected by reverberating waves inside the layer rather than geometric divergence. The reason is that at the early stage, the two interfaces travel only a short distance in the radial direction (approximately 22 mm) and thus geometric divergence produces a negligible influence. Hence, we can employ the 1-D theory of Liang & Luo (2021*a*) developed for the layer motion in planar geometry to predict the present gas layer motion. Considering there is a visible velocity difference ($\delta V = \Delta V_1 - \Delta V_2$) between the inner and outer interfaces (this ensures the mass conservation inside the layer), we introduce an average velocity for the present gas layer, which is defined as $V = (\Delta V_1 + \Delta V_2)/2$. Then, the 1-D theory of Liang & Luo (2021*a*) is adopted to calculate the average velocity of the gas layer. Under the incompressible flow assumption, the velocity difference between the inner and outer interfaces is $\delta V = Vd/R$ with d and R being the thickness and average radius of the layer, respectively. Provided with the values of δV and V, the velocities of the inner and outer interfaces can be readily obtained. As shown in figure 3(*a*), good agreement between theoretical prediction and experimental result for the trajectories of two interfaces is obtained.

At late stages, the inner and outer interfaces decelerate evidently, as shown in figure 3(*b*). This differs from the gas layer motion in planar geometry, where its two interfaces move uniformly when the reverberating waves are far away. To understand such an interface deceleration phenomenon, we consider 1-D Euler equations in a cylindrical coordinate system, which are written as

$$\left.\begin{aligned} \frac{\mathrm{D}\rho}{\mathrm{D}t} + \frac{1}{r}\frac{\partial (u_r r)}{\partial r} = 0, \\ \frac{\mathrm{D}u_r}{\mathrm{D}t} + \frac{1}{\rho}\frac{\partial p}{\partial r} = 0. \end{aligned}\right\} \tag{3.3}$$

Here, u_r refers to the velocity component in the radial direction, ρ to the density and p to the pressure. The symbol D denotes the material derivative. At late stages when the waves are far away from the gas layer, the flow can be assumed as incompressible (i.e. $\mathrm{D}\rho/\mathrm{D}t = 0$). Then, the mass conservation equation reduces to

$$\frac{\partial (u_r r)}{\partial r} = 0. \tag{3.4}$$

Further assuming the post-shock flow is steady, there is

$$\frac{\mathrm{D}(u_r r)}{\mathrm{D}t} = \frac{\partial (u_r r)}{\partial t} + u_r \frac{\partial (u_r r)}{\partial r} = 0. \tag{3.5}$$

Solving (3.5), we get

$$u_r = C/r, \tag{3.6}$$

where C is a constant independent of time and space. For an initial time t_0 at which $u_r(t_0) = u_0$ and $r(t_0) = r_0$, there is $C = u_0 r_0$. Then, the trajectory of a fluid element in divergent geometry can be derived as

$$r = \left[r_0^2 + 2C(t - t_0)\right]^{1/2}, \tag{3.7}$$

and the velocity is

$$u_r = C\left[r_0^2 + 2C(t - t_0)\right]^{-1/2}. \tag{3.8}$$

Equations (3.7) and (3.8) indicate that the increment of flow cross-section area can give rise to flow deceleration, which is qualitatively consistent with the interface deceleration observed in experiment. Nevertheless, (3.8) quantitatively underestimates the interface velocity at late stages, as shown in figure 3(*b*). This may be ascribed to the steady flow assumption adopted in our derivation process.

A key unsteady feature of the present flow is that the divergent shock becomes gradually weaker with time, producing a positive pressure gradient behind the shock wave in the radial direction. This may be a major factor causing the underestimation of (3.8). The following description gives the details regarding the treatment of post-shock pressure gradient. According to the Chester–Chisnell–Whitham (CCW) relation (Chester 1954; Chisnell 1957; Whitham 1958), the Mach number of a cylindrically divergent shock decreases with the radius r, which can be described as

$$\frac{2MdM}{(M^2 - 1)K(M)} + \frac{dr}{r} = 0, \tag{3.9}$$

where

$$K(M) = \left[\left(1 + \frac{2}{\gamma + 1}\frac{1 - \sigma^2}{\sigma}\right)\frac{2\sigma + 1 + M^{-2}}{2}\right]^{-1}, \tag{3.10}$$

with

$$\sigma = \sqrt{[(\gamma - 1)M^2 + 2]/[2\gamma M^2 - (\gamma - 1)]}. \tag{3.11}$$

Here, γ is the specific heat ratio of the gas. Provided the initial shock strength ($M = M_0$) at $r = r_0$, the divergent shock strength at an arbitrary time (or at an arbitrary position) can be readily obtained with (3.9). According to Rankine–Hugoniot conditions, the post-shock pressure can be calculated by

$$\frac{p_2}{p_1} = 1 + \frac{2\gamma}{\gamma + 1}(M^2 - 1). \tag{3.12}$$

Since the shock wave moves much faster than the interface, the post-shock pressure field is established in a very short time, during which the pressure at each local region can be assumed to be invariant. By incorporating the calculated pressure gradient into the momentum equation in (3.3), the influence of a non-uniform pressure field on the interface motion can be quantified. As shown in figure 3(*b*), (3.7) with the pressure gradient modification gives a good prediction of the interface motion for all gas layers. Particularly, the interface deceleration at late stages, which could cause RT instability/stability for an initially perturbed interface, is well reproduced by the theory. We close this section with a conclusion that we establish a 1-D theory to describe the motion of a gas layer in divergent geometry from early to late stages. This non-uniform motion constitutes the background flow for the development of a perturbed gas layer.

Case	Ma	d_0 (mm)	a_{01} (mm)	n	λ (mm)	a_{01}/λ	mfra (SF_6)	A	A^+	γ	c (m s^{-1})
1	1.27	10	2.0	24	39.3	0.051	0.989	0.66	0.69	1.099	145.1
2	1.27	20	2.0	24	39.3	0.051	0.989	0.66	0.69	1.096	144.9
3	1.25	30	2.0	24	39.3	0.051	0.972	0.64	0.67	1.109	149.6
4	1.27	20	1.0	24	39.3	0.025	0.987	0.66	0.69	1.097	145.7
5	1.25	20	3.0	24	39.3	0.076	0.986	0.65	0.69	1.097	145.5
6	1.27	20	2.0	36	26.2	0.076	0.995	0.67	0.70	1.094	142.5

Table 1. Detailed parameters corresponding to the initial conditions for each case. Note: a_{01} and n are the initial amplitude and azimuthal mode number of the inner interface, respectively; Ma refers to the Mach number of incident cylindrical shock; d_0 to the layer thickness; λ to the wavelength of the inner interface; mfra(SF_6) to the mass fraction of SF_6 inside the layer; A to the Atwood number; A^+ to the post-shock Atwood number; γ to the specific heat ratio inside the layer and c to the post-shock sound speed inside the layer.

3.2. *Quasi-two-dimensional experimental results and analysis*

Six kinds of SF_6 layers with various thicknesses, amplitudes and wavelengths of the inner interface are then considered. Detailed parameters corresponding to the initial conditions for each case are listed in table 1, where the Atwood number (A) is defined as $A = (\rho_2 - \rho_1)/(\rho_2 + \rho_1)$ with ρ_2 and ρ_1 being the gas densities inside and outside the gas layer, respectively. For cases 1–3, the average position of the inner interface is fixed at $R_{01} = 150$ mm and the outer interface takes various radii of $R_{02} = 160$, 170 and 180 mm, corresponding to the layer thicknesses of $d_0 = 10$, 20 and 30 mm, respectively. The amplitude-to-wavelength ratio of the inner interface is 0.051 by taking an initial amplitude $a_{01} = 2$ mm and an azimuthal mode number $n = 24$.

Developments of the wave patterns and interfacial morphologies for six cases are shown in figure 4. Since the evolution processes for these cases are qualitatively similar, we take case 2 as an example to detail the evolution process. At the beginning ($-20\,\mu$s), an incident cylindrical shock (ICS) together with the inner and outer interfaces of the gas layer can be clearly observed. The ICS has a cylindrical shape and also the inner (outer) interface presents an ideal single-mode (cylindrical) shape, which demonstrates good feasibility of the present experimental method. Later, ICS collides with the inner interface (air/SF_6), immediately bifurcating into a sine-like transmitted shock (TS_1) and a reflected shock (RS_1). During this process, the inner interface suffers a quick drop in amplitude due to shock compression. Later, driven by pressure disturbance and baroclinic vorticity, the amplitude of the inner interface increases persistently before the arrival of the rarefaction wave (RW_1). Subsequently, the disturbed TS_1 encounters the outer interface, generating a second transmitted shock (TS_2) that has a larger amplitude than TS_1. It indicates that the outer interface (SF_6/air) here serves as an 'amplifier' for the perturbation amplitude of a passing shock. During this process, TS_1 seeds a small positive perturbation on the outer interface. In this work, the amplitude of perturbation with the same phase as that of the inner interface is defined as positive, and otherwise negative. As time proceeds, TS_2 propagates downwards with its amplitude decaying gradually and finally recovers to a uniform cylindrical shock. To clearly show the layer evolution process, sketches of the wave patterns and interfacial morphologies at typical moments for case 2 are given in figure 5. In the following two subsections, we quantitatively discuss the instability growths at the inner and outer interfaces, respectively.

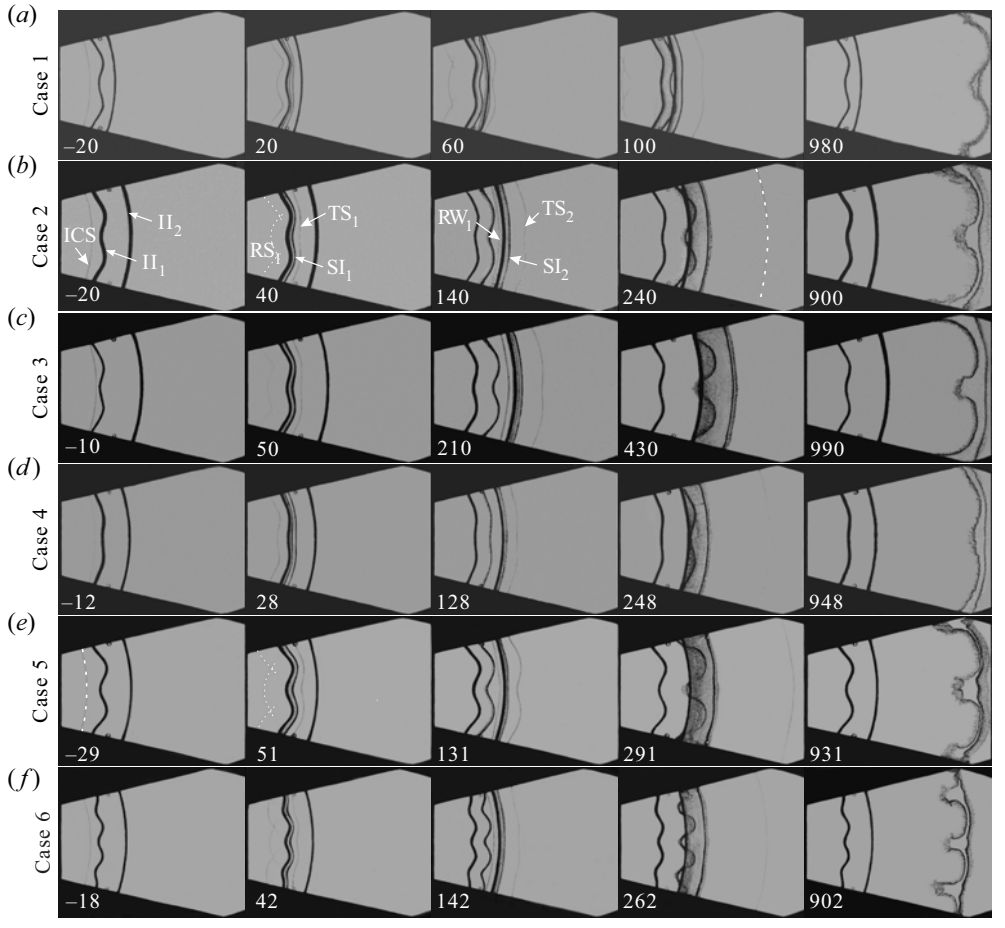

Figure 4. Schlieren images showing the developments of wave patterns and interfacial morphologies for all cases. ICS denotes the incident cylindrical shock and II_1 is the initial first interface. The other symbols are the same as those in figure 2. The numbers are in μs.

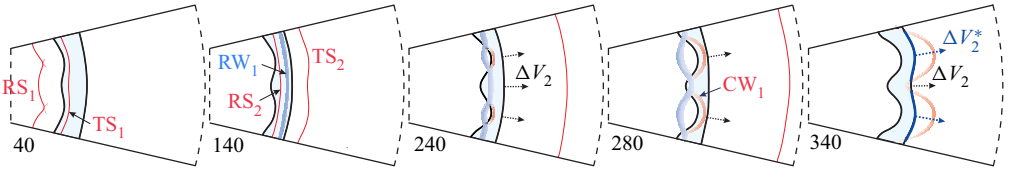

Figure 5. Sketches of the wave patterns and interface morphologies at typical moments for case 2. Here, ΔV_2 (ΔV_2^*) is the velocity of the outer interface after the impact of TS_1 (CW_1). The other symbols are the same as those in figure 4. The numbers are in μs.

3.2.1. *Instability growth at the inner interface*

Normalized variations of the amplitude of the inner interface versus time for all cases are plotted in figure 6. The interface amplitude is normalized as $\alpha = n(a_1 - a_1^+)/R_{01}$ and the time as $\tau = n\dot{a}_0(t - t_1^+)/R_{01}$. Here, a_1^+ refers to the post-shock amplitude of the inner interface and t_1^+ to the time just after the incident shock passes across the inner interface, and $\dot{a}_0$ denotes the perturbation growth rate shortly after the shock impact, which can be

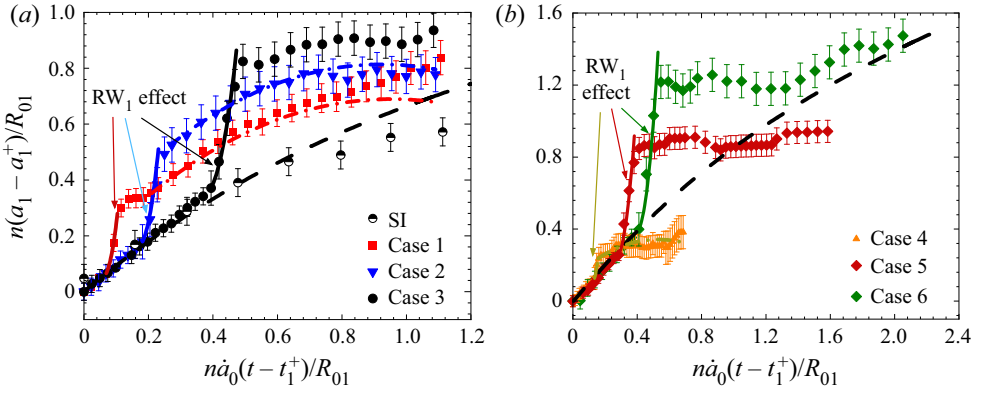

Figure 6. Normalized variations of the amplitude of the inner interface versus time for different cases. SI refers to the perturbation growth of a single air/SF_6 interface from Li *et al.* (2020). The dashed line refers to the prediction of Bell model, the dash–dotted line to the prediction of the Bell-RT model, and the solid line to the prediction of the Bell-RT-m model that considers the interface stretching and RT instability caused by RW_1.

Case	t_1^+ (μs)	a_1^+ (mm)	t_2^+ (μs)	a_2^+ (mm)	ΔV_1 (m s^{-1})	ΔV_2 (m s^{-1})	$\dot{a}_0$ (m s^{-1})
1	20.5	1.42	60.5	0.40	94.0	114.5	7.2
2	20.1	1.42	120.1	0.16	86.6	103.5	7.1
3	29.6	1.42	169.6	0.10	85.7	108.5	7.7
4	7.9	0.52	107.9	0.04	91.6	107.6	4.2
5	10.9	2.10	110.9	0.35	84.2	105.6	9.9
6	22.0	1.44	122.0	0.04	86.8	103.9	9.5

Table 2. The post-shock parameters for six cases. Note: t_i^+ refers to the time just after the shock crosses the inner ($i = 1$) or outer ($i = 2$) interface; a_i^+ to the corresponding amplitude at t_i^+; ΔV_i to the post-shock velocity of the interface; $\dot{a}_0$ to the growth rate of the inner interface at t_i^+.

obtained by a linear fit of experimental data, as listed in table 2. At the early stage, the dimensionless amplitude histories collapse quite well for all cases and also are in good agreement with the RM instability growth at a single interface. When RW_1 interacts with the evolving inner interface, RT instability and interface stretching begin to play a role, causing a quick rise in perturbation growth rate. Later, the perturbation growth rate decays continuously with time. It is found that a thicker gas layer results in a larger extent that the RW_1 promotes the instability growth at the inner interface. For case 1 with a thinner gas layer, RW_1 arrives at the inner interface earlier and thus the interface presents a larger amplitude than thicker cases at the early stage. Nevertheless, at late stages, the inner interface presents a smaller perturbation amplitude than that of thicker layers. For cases 3–6, the perturbation growth rate approaches zero at late stages (i.e. the instability freezes out Mikaelian 1985). It can be generally found that the existence of the outer interface promotes the instability growth at the inner interface as compared to RM instability at an isolated single-mode interface (Li *et al.* 2020).

The instability growth at the inner interface can be generally divided into three stages: early stage, intermediate stage (i.e. wave interaction stage) and late stage. At the early stage ($t < t_1^{RW}$), the perturbation growths for various-thickness layers collapse quite well, which indicates a negligible interface coupling effect. Thus, the instability growth at this stage

can be described by the linear theory for cylindrical RM instability at an isolated interface. According to Bell (1951) and Ding *et al.* (2017*b*), the growth of cylindrical RM instability at a single-mode interface can be described as

$$\frac{1}{R^2}\frac{\mathrm{d}}{\mathrm{d}t}\left(R^2\dot{a}\right) - (nA-1)\frac{\ddot{R}}{R}a = 0, \tag{3.13}$$

where $\dot{a}$ is the first derivative of amplitude with time and $\ddot{R}$ is the second derivative of radius with time. Treating the shock impact as an impulse function (i.e. $\ddot{R} = \delta(t)\Delta V$), the perturbation amplitude at an arbitrary time t can be obtained by integrating (3.13),

$$a(t) = a_0^+ + \dot{a}_0 R_0^2 \int_{t_0^+}^{t} \frac{1}{R^2(t')}\,\mathrm{d}t' + (nA-1)\int_{t_0^+}^{t}\left(\frac{1}{R^2(t')}\int_{t_0^+}^{t'} aR\ddot{R}\,\mathrm{d}t''\right)\mathrm{d}t'. \tag{3.14}$$

Here, t_0^+ refers to the time just after the shock passage and $\dot{a}_0$ to the initial growth rate at t_0^+, which can be obtained by a linear fit of experimental data (shown in table 2). The first term on the right-hand side of (3.14) stands for the post-shock amplitude, the second term for pure RM instability combined with the geometric divergence effect and the third term for the perturbation growth associated with RT instability/stability. For brevity, (3.14) is termed as the Bell-RT model. Dynamics of an unperturbed gas layer in § 3.1 shows that the inner interface moves at a constant speed at the early stage. For this situation, the third term equals zero and (3.14) is called the Bell model. As shown in figure 6(*a*), the Bell model gives a reasonable prediction of the perturbation growth at the early stage for all cases. This further confirms that the interface coupling effect is very weak at the early stage.

At the intermediate stage, RW_1 accelerates the inner interface and thus the Bell model deviates from the experimental results. We realise that RW_1 does not only accelerate but also stretches the inner interface. In the following analysis, we take both RT instability (caused by interface acceleration) and interface stretching into account. First, we consider the stretching effect. Since the interface stretching process lasts for a short period of time, during which the interface travels a short distance, this process can be approximately considered as that happening in a planar geometry. This approximation can simplify the analysis. As sketched in figure 7, RW_1 first crosses the peak of the inner interface (point A), causing a local velocity rise, whereas the trough of the interface (point B) moves at its original speed before the arrival of RW_1. Such a velocity difference produces a quick increment in interface amplitude, which is termed as the stretching effect. The stretching process involves three phases: RW_1 passes across point A ($t_1^{RW} \sim t_2^{RW}$), RW_1 tail leaves point A but its head has not arrived at point B ($t_2^{RW} \sim t_3^{RW}$), and RW_1 passes across point B ($t_3^{RW} \sim t_4^{RW}$). Time duration for the first phase is $\Delta t_1 = t_2^{RW} - t_1^{RW}$, for the second phase is $\Delta t_2 = t_3^{RW} - t_2^{RW}$, and for the third phase is $\Delta t_3 = t_4^{RW} - t_3^{RW}$. Obviously, there is $\Delta t_1 = \Delta t_3$.

To simplify the analysis, we assume the interface undergoes a constant acceleration (g) during the passage of RW_1. The constant acceleration is $g = (\Delta V_1^* - \Delta V_1)/\Delta t_1$, which can be estimated by the 1-D theory developed in § 3.1. The layer thickness at the time when TS_1 encounters the outer interface is denoted by d^*, which can be readily obtained. Also, the width of RW_1 (defined as the distance between its head and tail) at the moment when it encounters the inner interface is $L = (\gamma+1)(\Delta V_2 - \Delta V_1)d^*/(2c)$, where γ and c denote the specific heat ratio and sound speed behind TS_1 inside the gas layer, respectively. For the first/third phase, the interface motion satisfies $g(\Delta t_1)^2/2 + c\Delta t_1 = L$.

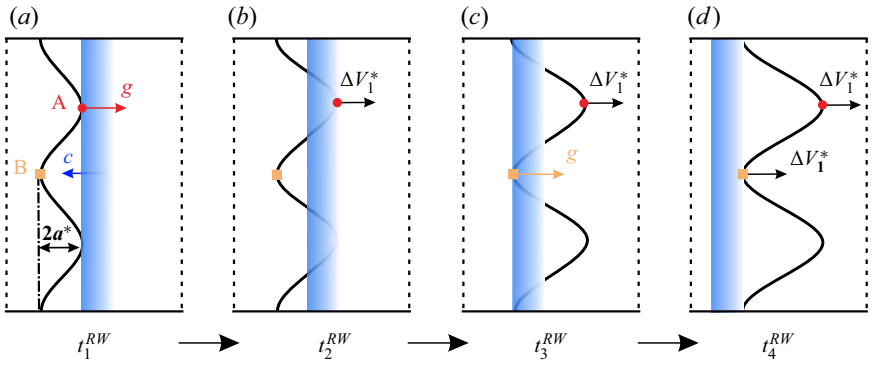

Figure 7. Sketches showing the interface stretching process by rarefaction wave RW_1.

Case	a_1^* (mm)	d^* (mm)	L (mm)	ΔV_1^* (m s^{-1})	Δt_1 (μs)	Δt_2 (μs)	g (m s^{-2})	$\dot{a}_s$ (m s^{-1})
1	1.83	5.6	0.83	118.0	5.3	19.5	4 540 000	9.9
2	2.54	11.4	1.39	110.9	8.9	25.5	2 750 000	9.7
3	3.74	17.4	2.79	108.1	17.2	31.4	1 300 000	9.5
4	1.31	10.8	1.24	112.9	7.9	9.5	2 690 000	7.3
5	3.70	11.7	1.80	106.5	11.3	38.5	1 970 000	11.1
6	3.10	11.5	1.44	108.3	9.3	33.4	2 310 000	9.8

Table 3. The relevant parameters for cases 1–6. Note: a_1^* is the inner interface amplitude just before the arrival of RW_1; d^* is the layer thickness at the time when TS_1 encounters the outer interface; L is the width between the head and tail of RW_1 when it arrives at the inner interface; ΔV_1^* is the velocity of the inner interface after the impact of RW_1; Δt_1 (Δt_2) is the time of the first (second) stage for RW_1 interacting with the perturbed inner interface; g is the acceleration of the inner interface caused by RW_1; and $\dot{a}_s$ is the average growth rate caused by interface stretching.

Combining the above equations, Δt_1 and g can be readily calculated. For the second phase, there is $c\Delta t_2 = 2a_1^* - c\Delta t_1$, where a_1^* is the amplitude of the inner interface immediately before the impact of RW_1. Analytical solutions for the key parameters are summarized as

$$\left.\begin{aligned} \Delta t_1 = \Delta t_3 = 2L/\left(2c + \Delta V_1^* - \Delta V_1\right), \\ \Delta t_2 = \left(2a_1^* - c\Delta t_1\right)/c, \\ g = \left(\Delta V_1^* - \Delta V_1\right)/\Delta t_1. \end{aligned}\right\} \tag{3.15}$$

The above parameters are calculated and listed in table 3. With these values, the displacement difference between points A and B at the stretching stage is

$$\Delta x = (\Delta V_1^* - \Delta V_1)(\Delta t_1 + \Delta t_2). \tag{3.16}$$

Thus, the average growth rate caused by interface stretching is

$$\dot{a}_s = \Delta x/[2(\Delta t_1 + \Delta t_2 + \Delta t_3)]. \tag{3.17}$$

Next, we consider the effect of RT instability caused by RW_1 on the perturbation growth by incorporating the average acceleration g calculated by (3.15) into the Bell-RT model. Finally, a modified Bell-RT model (Bell-RT-m) accounting for both the RT effect and

interface stretching can be proposed, which is written as

$$a(t) = a_0^+ + \dot{a}_0 R_0^2 \int_{t_0^+}^{t} \frac{1}{R^2(t')}\,\mathrm{d}t' + (nA - 1)\int_{t_0^+}^{t}\left(\frac{1}{R^2(t')}\int_{t_0^+}^{t'} aR\ddot{R}\,\mathrm{d}t''\right)\mathrm{d}t' + \dot{a}_s(t - t_1^{RW}). \tag{3.18}$$

Note, (3.18) is valid only during the interaction of RW_1 with the inner interface (i.e. $t_1^{RW} < t < t_4^{RW}$). As shown in figure 6, the Bell-RT-m model well reproduces the quick instability growth at the wave interaction stage for all cases, which demonstrates its validity. It is found that for cases with a thicker gas layer or a larger amplitude-to-wavelength ratio, RW_1 promotes the instability growth to a larger extent. This is also confirmed by the Bell-RT-m model. The reason is discussed below. As the layer thickness or the initial amplitude-to-wavelength ratio becomes larger, the interface amplitude experiences a longer period of linear growth or a faster linear growth. As a result, the inner interface possesses a larger amplitude just before the arrival of RW_1, giving rise to stronger RT and stretching effects. It is also found that RW_1 promotes the growth of divergent RM instability to a larger extent as compared to the planar counterpart (Liang & Luo 2021*a*). This is ascribed to an overall slower growth of divergent RM instability caused by geometric expansion than the planar counterpart.

At late stages, reverberating waves inside the layer are negligibly weak and also the inner interface decelerates evidently due to geometric divergence, producing RT stability. Thus, the instability growth at the late stage is dominated by RM instability and RT stability. It has been reported by Li *et al.* (2020) that for divergent RM instability at an isolated interface, nonlinearity is very weak and produces a negligible influence on the growth of overall amplitude. Hence, the linear Bell-RT model can be adopted to predict the growth of divergent RM instability at late stages. Here, we first calculate the interface deceleration according to the 1-D theory developed in § 3.1, and then substitute the calculated deceleration into the Bell-RT model. In this way, the Bell-RT model gives a good prediction of the perturbation growth for cases 1, 2 and 4, as shown in figure 6. Nevertheless, it fails to reproduce the very slow instability growth (even the instability freeze-out) after the impact of RW_1 for cases 3, 5 and 6. This is ascribed to relatively stronger nonlinearity in these cases in which the interface amplitude is quickly amplified by RW_1. It should be noted that for case 1 with a thin layer, the perturbation amplitude continues increasing after reaching saturation ($\tau > 0.8$) due to the increasing interface coupling effect, which is not considered by the Bell-RT model.

3.2.2. *Instability growth at the outer interface*

Variations of the amplitude of the outer interface versus time for all cases are plotted in figure 8. Unlike the inner interface, the outer interface presents no perturbation initially. Thus, it is difficult to choose appropriate reference quantities for normalization. This is the reason why figure 8 is plotted in physical units. The perturbation growths for various-thicknesses cases are distinctly different. Specifically, for case 1 with a thin layer, the transmitted shock TS_1 presents a larger perturbation amplitude immediately before it encounters the outer interface (SF_6/air). Thus, a relatively larger perturbation is seeded at the outer interface by the rippled TS_1. As CW_1 impacts the outer interface, such a perturbation experiences a quick growth. At late stages, the perturbation amplitude continues growing due to interface coupling. Differently, for thicker gas layers (cases 2 and 3), TS_1 travels a longer distance to arrive at the outer interface and its amplitude undergoes a greater degree of decay during this process. As a consequence, only a subtle

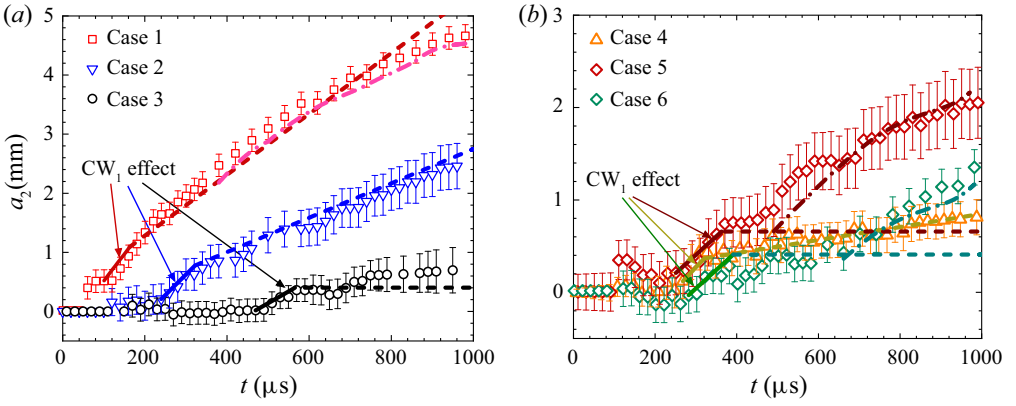

Figure 8. Variations of the amplitude of the outer interface versus time. The solid line refers to the model prediction considering the effect of CW_1 and interface coupling, the dashed line to model prediction considering interface coupling effect and the dash–dotted line to the prediction of (3.27).

perturbation is produced at the outer interface by TS_1, even for case 5 with an initial larger perturbation at the inner interface. This differs greatly from convergent RM instability (Ding *et al.* 2019), where the distorted transmitted shock keeps invariant or even increases in amplitude during the propagation process, and consequently seeds a considerably large perturbation at the downstream interface. Afterwards, the growth rate of the interface amplitude remains nearly zero before the arrival of CW_1 (i.e. freezes out). The reason for the instability freeze-out is given below. First, the uniform TS_1 in cases 2 and 3 produces no velocity perturbation, continuous pressure perturbation and baroclinic vorticity (i.e. there are no forces driving the instability growth). Second, even though there is a small perturbation produced by TS_1, its amplitude would reduce due to geometric divergence. Also, after CW_1 encounters the outer interface, the interface amplitude experiences a considerably quick growth. Later, as the two interfaces become closer to each other, the interface coupling effect becomes dominant, which continuously promotes the instability growth at the outer interface.

The CW_1 and interface coupling are major factors driving the instability growth at the outer interface. Here, we first give a quantitative analysis on the effect of CW_1 on the instability growth. The mechanism for the perturbation growth induced by CW_1 is illustrated in figure 5. Considering the thickness of the gas layer is much smaller than its radius (i.e. $d \ll R$), waves inside the layer vary slightly in speed and thus can be assumed to be of constant strengths (Sun *et al.* 2020). The velocity jump ($\Delta V_{cw} \approx 8$ m s^{-1}) of the outer interface caused by CW_1 for the unperturbed case can be adopted to approximate that of a perturbed layer. According to a simple analysis, the amplitude of the distorted CW_1 is found to be nearly twice the amplitude of the inner interface at the time when RW_1 encounters the inner interface (a_1^*). Then, the time duration for the distorted CW_1 passing through the perturbed outer interface is $\Delta t_{cw} = (4a_1^* - 2a_2^*)/c$, where a_2^* is the amplitude of the outer interface just before its collision with CW_1. The calculated results for all cases are listed in table 4. Hence, the average growth rate of the outer interface caused by CW_1 is $\dot{a}_{cw} = \Delta V_{cw}/2$.

After CW_1 moves away, the amplitude of the outer interface grows persistently. This is mainly ascribed to the interface coupling effect. For the evolution of a gas layer with two interfaces, Mikaelian (1995) proposed a linear model (MIK model) to quantify the

Case	a_2^* (mm)	Δt_{cw} (μs)	$\dot{a}_1^{cou}$ (m s^{-1})	$\sin\beta$	$\dot{a}_2^{cou}$ (m s^{-1})
1	0.52	43.3	6.9 ± 0.6	0.75	5.2 ± 0.45
2	0.21	67.2	6.2 ± 0.3	0.47	5.9 ± 0.14
3	0.02	99.7	0	0.34	0
4	0.22	32.9	1.5 ± 1.0	0.47	0.7 ± 0.47
5	0.13	99.9	0	0.47	0
6	−0.18	89.5	0	0.28	0

Table 4. The relevant parameters for the interaction between CW_1 and the outer interface. Note: a_2^* is the perturbation amplitude of the outer interface just before the arrival of CW_1; Δt_{cw} is the duration for the perturbed CW_1 passing through the outer interface; β is the coupling angle; and $\dot{a}_1^{cou}$ ($\dot{a}_2^{cou}$) represents the growth rate of the inner (outer) interface.

influence of interface coupling on the instability growth, which is written as

$$\left.\begin{aligned} \dot{a}_1^{cou} &= \frac{\Delta V \Gamma^2}{\cos\beta}\left(a_{01} - a_{02}\sin\beta\right), \\ \dot{a}_2^{cou} &= -\frac{\Delta V \Gamma^2}{\cos\beta}\left(a_{02} - a_{01}\sin\beta\right), \end{aligned}\right\} \tag{3.19}$$

where

$$\left.\begin{aligned} \Gamma^2 &\equiv k(D-1)/\left[1 + D^2 + 2D\coth(kd)\right]^{1/2}, \\ \sin\beta &= (2W_1/W_2)/\left[1 + (W_1/W_2)^2\right], \\ W_1/W_2 &= 1 + ST + (S/D)\left\{1 + \left[1 + D^2 + 2D\coth(kd)\right]^{1/2}\right\}, D = \rho_2/\rho_1, \\ S &\equiv \sinh(kd), \quad T \equiv \tanh(kd/2). \end{aligned}\right\} \tag{3.20}$$

Here, a_{0i} and $\dot{a}_i^{cou}$ (i=1 or 2 for the inner or outer interface) are the initial perturbation amplitude and perturbation growth rate, respectively, $k = n/R$ is the perturbation wave number, and ΔV is the velocity of the gas layer. When the layer thickness (d) tends to infinity, the interface coupling angle (β) that represents the strength of interface coupling tends to zero. Thus, (3.19) reduces to the impulsive model for each interface, i.e. the developments of the two interfaces are decoupled.

To clearly show the interface coupling effect on the growths of the inner and outer interfaces, we calculate the ratio of the growth rate predicted by the MIK model to impulsive model ($\dot{a}_i^{SI}$),

$$\left.\begin{aligned} c_1 &= \frac{\dot{a}_1^{cou}(d)}{\dot{a}_1^{SI}} = \frac{\Gamma^2(d)}{\Gamma_0^2}\left(\frac{1}{\cos\beta} - \frac{a_2^+}{a_1^+}\tan\beta\right), \\ c_2 &= \frac{\dot{a}_2^{cou}(d)}{\dot{a}_2^{SI}} = \frac{\Gamma^2(d)}{\Gamma_0^2}\left(\frac{1}{\cos\beta} - \frac{a_1^+}{a_2^+}\tan\beta\right). \end{aligned}\right\} \tag{3.21}$$

Variations of c_1 and c_2 with the layer thickness are plotted in figure 9. As we can see, for the present gas layer (inner interface is perturbed and outer interface is uniform),

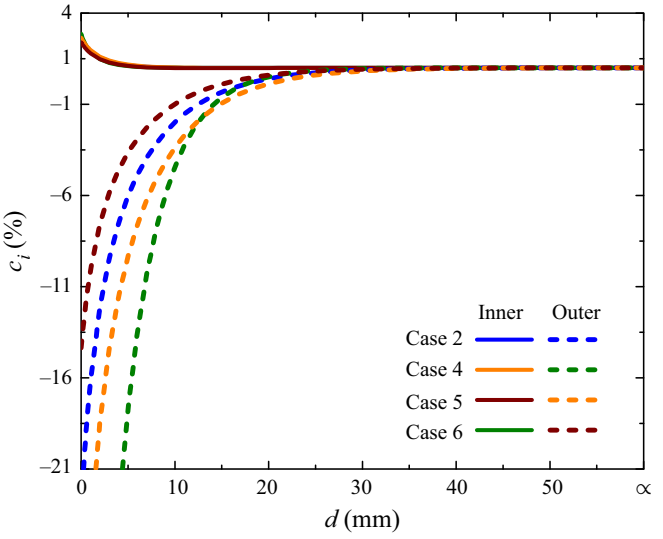

Figure 9. Variations of c_1 and c_2 with the layer thickness.

interface coupling produces a very weak influence on the inner interface development, but a significant influence on the outer interface. This reasonably explains the finding that the linear Bell model gives a good prediction of the inner perturbation development in experiment. According to (3.19), for $a_{02} = 0$, the growth rate of the outer interface can be rewritten as

$$\dot{a}_2^{cou} = \dot{a}_1^{cou} \sin\beta. \tag{3.22}$$

Provided with the perturbation growth rate of the inner interface and the thickness of the unperturbed layer (measured from experiment), the growth rate of the outer interface can be obtained.

Since nonlinearity is very weak for the divergent RM instability considered in this work, the growth rate of the outer interface can be obtained by a linear superposition of the two components caused by interface coupling and wave influence,

$$\dot{a}_2 = \dot{a}^{cw} + \dot{a}_2^{cou}. \tag{3.23}$$

As shown in figure 8, (3.23) gives a reasonable prediction of the perturbation growth at the wave-affecting stage for all cases. After this stage ($\dot{a}^{cw} = 0$), the amplitude growth of the outer interface can also be well predicted by the model for cases 1–4. However, for cases 5 and 6, the model prediction deviates greatly from the experimental results. Specifically, at late stages the perturbation growth of the inner interface freezes out (i.e. the growth rate is zero), and thus the growth rate of the outer interface should be zero as indicated by (3.22). This is apparently inconsistent with the experimental observation. A major reason is that for cases 5 and 6, the amplitude of the inner interface is larger than the layer thickness at late stages (931, 902 μs in figure 4), i.e. the two interfaces coalesce. For this situation, the original MIK model is invalid.

Here, a primary analysis based on the volume equivalence between perturbed and unperturbed layers is given. As found in § 3.1, when an unperturbed layer moves outwards, it becomes gradually thinner, which can be readily measured from experiment. We realize that the volume of a perturbed layer is equal to that of the unperturbed one during the motion process under the incompressible flow assumption. As sketched in figure 10, for

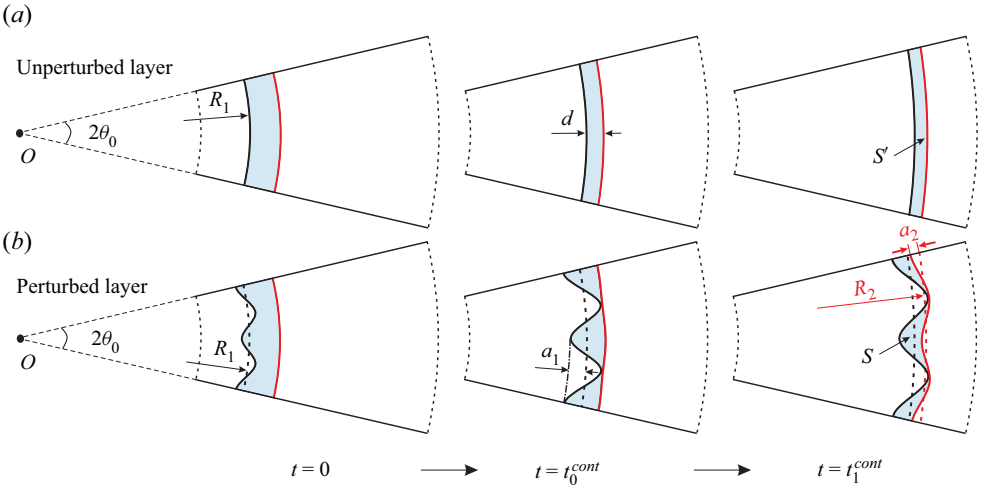

Figure 10. Schematic diagrams showing the gas layer deformation for unperturbed and perturbed cases.

a gas layer with a perturbed inner interface and an unperturbed outer interface, as the layer moves outward, the layer thickness decreases continuously. After a certain critical time (t_0^{cont}) at which the amplitude of the inner interface is equal to the layer thickness, the bubble of the inner interface penetrates into the outer interface (t_1^{cont}), forming a perturbation at the outer interface that has the same phase as the inner interface. Assuming the inner and outer interfaces are in the form of cosine perturbation at late stages, i.e.

$$\left.\begin{aligned} r_1 &= R_1 - a_1 \cos n\theta, \\ r_2 &= R_2 - a_2 \cos n\theta, \end{aligned}\right\} \tag{3.24}$$

where a_1 (a_2) is the amplitude of the inner (outer) interface, $R_2 = R_1 + a_1 - a_2$, then the fluid area between the two perturbed interfaces is

$$S = \int_{-\theta_0}^{\theta_0} \mathrm{d}\theta \int_{r_1}^{r_2} r\,\mathrm{d}r = \left[\frac{3}{2}a_2^2 - 2\left(R_1 + a_1\right)a_2 + 2R_1 a_1 + \frac{1}{2}a_1^2\right]\theta_0, \tag{3.25}$$

and the fluid area S' contained in the corresponding undisturbed gas layer is

$$S' = \int_{-\theta_0}^{\theta_0} \mathrm{d}\theta \int_{R_1}^{R_1+d} r\,\mathrm{d}r = \left(2R_1 d + d^2\right)\theta_0. \tag{3.26}$$

For the perturbed and unperturbed cases, their areas should be equal at an arbitrary time. By combining (3.25) and (3.26), the relationship between the amplitude of the outer interface a_2 and the amplitude of the inner interface a_1 can be obtained as

$$a_2 = \frac{2\left(R_1 + a_1\right) - \sqrt{6\left(R_1 + d\right)^2 - 2\left(R_1 + a_1\right)^2 + 3a_1^2}}{3}. \tag{3.27}$$

Equation (3.27) indicates that as the amplitude of the inner interface becomes larger than the layer thickness, it greatly increases the outer perturbation development. To the best of the authors' knowledge, such a perturbation growth that exists uniquely in divergent multi-layer RM instability is reported for the first time. For cases 1, 5 and 6, where the layer

thickness is smaller than the amplitude of the inner interface, substituting the amplitude and radius of the inner interface as well as the layer thickness (obtained from experiment) into (3.27), the amplitude growth of the outer interface at late stages is obtained. As shown in figure 8, (3.27) gives a reasonable prediction of the late-stage instability growth at the outer interface for these three cases. This indicates that interface coupling plays a crucial role in the development of the outer interface at late stages although it produces a much weaker effect on the development of the inner interface. It should be mentioned that the present study is mainly focused on the RM instability induced by a weak shock. For the strong shock case, a compressibility effect becomes evident, producing possibly new flow structures and phenomena (Ranjan *et al.* 2007, 2008).

4. Conclusions

Experiments of divergent RM instability at a perturbed heavy gas layer (a sinusoidal inner interface and a circular outer interface) are realized in a novel shock tube designed based on shock dynamics theory. An existing soap-film technique is extended to generate gas layers with controllable shape and thickness. The dynamics of an unperturbed gas layer is first examined. It is found that differing from the layer motion in planar and convergent geometries, the gas layer in divergent geometry becomes increasingly thinner with time. The inner and outer interfaces of the layer move uniformly at the early stage and decelerate evidently at late stages. A general 1-D theory that takes the influences of waves and post-shock non-uniform pressure field into account is established, which gives a good prediction of the layer motion in divergent geometry from early to late stages.

Six types of perturbed SF_6 layers with different thicknesses and shapes surrounded by air are then considered. High-quality schlieren images are obtained, which clearly reveal the wave evolution and interface deformation. The instability growth at the inner interface involves three stages: early stage, intermediate stage and late stage. At the early stage, the perturbation growths for various-thickness layers collapse quite well, which indicates a negligible interface coupling effect. Thus, the Bell model for cylindrical RM instability at an isolated interface can be adopted to describe the perturbation growth. At the intermediate stage (i.e. during the interaction of RW_1 with inner interface), the perturbation growth rate experiences a quick rise due to the presence of RT instability and interface stretching. A modified Bell-RT model accounting for both RT instability and interface stretching is established, which well reproduces the quick instability growth at this stage for all cases. Both theoretical prediction and experimental result indicate that a thicker gas layer results in the larger extent that RW_1 promotes the instability growth. It is also found that RW_1 promotes the growth of divergent RM instability to a larger extent than the planar counterpart (Liang & Luo 2021*a*) due to the overall slower growth of divergent RM instability caused by geometric expansion. At late stages, reverberating waves inside the layer are negligibly weak and the instability growth is dominated by RM instability and RT stability. For cases with strong nonlinearity, the instability nearly freezes out at the late stage, which is ascribed to the counteraction between the positive growth associated with RM instability and the negative growth associated with geometric divergence and RT stability.

Compression wave CW_1 and interface coupling are major factors driving the instability growth at the outer interface. As the distorted transmitted shock TS_1 passes across the uniform outer interface, it seeds a small perturbation at the outer interface. This seeded perturbation is smaller than the counterpart in planar and convergent geometries because the amplitude of TS_1 decays more quickly in divergent geometry. Then, the outer interface amplitude remains nearly invariant until the arrival of CW_1. As CW_1 encounters the outer

interface, the interface amplitude experiences a quick growth. Later, as the two interfaces become close to each other, interface coupling effect becomes dominant, significantly promoting the development of the outer interface. A modified MIK model (Mikaelian 1995) that takes the influences of CW_1 and interface coupling into account is developed, which gives a good prediction of the instability growth. For cases where the inner interface amplitude is larger than the layer thickness, a new interface coupling mechanism that exists uniquely in divergent geometry dominates the development of the outer interface. The finding in this work provides deep insights into divergent RM instability at multiple interfaces, which is useful for understanding the hydrodynamic instabilities in ICF and supernova explosion.

Funding. This work was supported by the National Natural Science Foundation of China (nos. 12122213, 12072341, 91952205 and 12027801).

Declaration of interests. The authors report no conflict of interest.

Author ORCIDs.
Juchun Ding https://orcid.org/0000-0001-6578-1694;
Ting Si https://orcid.org/0000-0001-9071-8646;
Xisheng Luo https://orcid.org/0000-0002-4303-8290.

References

Arnett, W.D., Bahcall, J.N., Kirshner, R.P. & Woosley, S.E. 1989 Supernova 1987A. *Annu. Rev. Astron. Astrophys.* **27**, 629–700.

Bell, G.I. 1951 Taylor instability on cylinders and spheres in the small amplitude approximation. Report No. LA-1321. Los Alamos Scientific Laboratory of the University of California.

Betti, R. & Hurricane, O.A. 2016 Inertial-confinement fusion with lasers. *Nat. Phys.* **12** (5), 435–448.

Biamino, L., Jourdan, G., Mariani, C., Houas, L., Vandenboomgaerde, M. & Souffland, D. 2015 On the possibility of studying the converging Richtmyer–Meshkov instability in a conventional shock tube. *Exp. Fluids* **56** (2), 1–5.

Brouillette, M. 2002 The Richtmyer–Meshkov instability. *Annu. Rev. Fluid Mech.* **34**, 445–468.

Chester, W. 1954 The quasi-cylindrical shock tube. *Phil. Mag.* **45**, 1293–1301.

Chisnell, R.F. 1957 The motion of a shock wave in a channel, with applications to cylindrical and spherical shock waves. *J. Fluid Mech.* **2**, 286–298.

Cohen, R.D. 1991 Shattering of a liquid drop due to impact. *Proc. R. Soc. Lond.* A **435**, 483–503.

Dimonte, G. & Ramaprabhu, P. 2010 Simulations and model of the nonlinear Richtmyer–Meshkov instability. *Phys. Fluids* **22**, 014104.

Dimotakis, P.E. & Samtaney, R. 2006 Planar shock cylindrical focusing by a perfect-gas lens. *Phys. Fluids* **18**, 031705.

Ding, J., Li, J., Sun, R., Zhai, Z. & Luo, X. 2019 Convergent Richtmyer–Meshkov instability of heavy gas layer with perturbed outer interface. *J. Fluid Mech.* **878**, 277–291.

Ding, J., Si, T., Chen, M., Zhai, Z., Lu, X. & Luo, X. 2017*a* On the interaction of a planar shock with a three-dimensional light gas cylinder. *J. Fluid Mech.* **828**, 289–317.

Ding, J., Si, T., Yang, J., Lu, X., Zhai, Z. & Luo, X. 2017*b* Measurement of a Richtmyer–Meshkov instability at an air-SF_6 interface in a semiannular shock tube. *Phys. Rev. Lett.* **119** (1), 014501.

Epstein, R. 2004 On the Bell–Plesset effects: the effects of uniform compression and geometrical convergence on the classical Rayleigh–Taylor instability. *Phys. Plasmas* **11** (11), 5114–5124.

Groom, M. & Thornber, B. 2021 Reynolds number dependence of turbulence induced by the Richtmyer–Meshkov instability using direct numerical simulations. *J. Fluid Mech.* **908**, A31.

Henry de Frahan, M.T., Movahed, P. & Johnsen, E. 2014 Numerical simulations of a shock interacting with successive interfaces using the Discontinuous Galerkin method: the multilayered Richtmyer–Meshkov and Rayleigh–Taylor instabilities. *Shock Waves* **25**, 329–345.

Hosseini, S.H.R., Ogawa, T. & Takayama, K. 2000 Holographic interferometric visualization of the Richtmyer–Meshkov instability induced by cylindrical shock waves. *J. Vis.* **2** (3–4), 371–380.

Jacobs, J.W., Jenkins, D.G., Klein, D.L. & Benjamin, R.F. 1995 Nonlinear growth of the shock-accelerated instability of a thin fluid layer. *J. Fluid Mech.* **295**, 23–42.

KURANZ, C.C., *et al.* 2018 How high energy fluxes may affect Rayleigh–Taylor instability growth in young supernova remnants. *Nat. Commun.* **9**, 1564.

LEI, F., DING, J., SI, T., ZHAI, Z. & LUO, X. 2017 Experimental study on a sinusoidal air/SF_6 interface accelerated by a cylindrically converging shock. *J. Fluid Mech.* **826**, 819–829.

LI, M., DING, J., ZHAI, Z., SI, T., LIU, N., HUANG, S. & LUO, X. 2020 On divergent Richtmyer–Meshkov instability of a light/heavy interface. *J. Fluid Mech.* **901**, A38.

LI, X., FU, Y., YU, C. & LI, L. 2022 Statistical characteristics of turbulent mixing in spherical and cylindrical converging Richtmyer–Meshkov instabilities. *J. Fluid Mech.* **928**, A10.

LIANG, Y., LIU, L., ZHAI, Z., DING, J., SI, T. & LUO, X. 2021 Richtmyer–Meshkov instability on two-dimensional multi-mode interfaces. *J. Fluid Mech.* **928**, A37.

LIANG, Y., LIU, L., ZHAI, Z., SI, T. & WEN, C. 2020 Evolution of shock-accelerated heavy gas layer. *J. Fluid Mech.* **886**, A7.

LIANG, Y. & LUO, X. 2021*a* On shock-induced heavy-fluid-layer evolution. *J. Fluid Mech.* **920**, A13.

LIANG, Y. & LUO, X. 2021*b* Shock-induced dual-layer evolution. *J. Fluid Mech.* **929**, R3.

LIANG, Y. & LUO, X. 2022 On shock-induced light-fluid-layer evolution. *J. Fluid Mech.* **933**, A10.

LIU, L., LIANG, Y., DING, J., LIU, N. & LUO, X. 2018 An elaborate experiment on the single-mode Richtmyer–Meshkov instability. *J. Fluid Mech.* **853**, R2.

LOMBARDINI, M., PULLIN, D.I. & MEIRON, D.I. 2014 Turbulent mixing driven by spherical implosions. Part 2. Turbulence statistics. *J. Fluid Mech.* **748**, 113–142.

LUO, X., ZHANG, F., DING, J., SI, T., YANG, J., ZHAI, Z & WEN, C. 2018 Long-term effect of Rayleigh–Taylor stabilization on converging Richtmyer–Meshkov instability. *J. Fluid Mech.* **849**, 231–244.

MESHKOV, E.E. 1969 Instability of the interface of two gases accelerated by a shock wave. *Fluid Dyn.* **4**, 101–104.

MIKAELIAN, K.O. 1985 Richtmyer–Meshkov instabilities in stratified fluids. *Phys. Rev.* A **31**, 410–419.

MIKAELIAN, K.O. 1995 Rayleigh–Taylor and Richtmyer–Meshkov instabilities in finite-thickness fluid layers. *Phys. Fluids* **7** (4), 888–890.

MILES, A.R., EDWARDS, M.J., BLUE, B., HANSEN, J.F., ROBEY, H.F., DRAKE, R.P., KURANZ, C. & LEIBRANDT, D.R. 2004 The effects of a short-wavelength mode on the evolution of a long-wavelength perturbatoin driven by a strong blast wave. *Phys. Plasmas* **11**, 5507–5519.

MOHAGHAR, M., CARTER, J., PATHIKONDA, G. & RANJAN, D. 2019 The transition to turbulence in shock-driven mixing: effects of Mach number and initial conditions. *J. Fluid Mech.* **871**, 595–635.

MUSCI, B., PETTER, S., PATHIKONDA, G., OCHS, B. & RANJAN, D. 2020 Supernova Hydrodynamics: a lab-scale study of the blast-driven instability using high-speed diagnostics. *Astrophys. J.* **896** (2), 92.

PENG, N., YANG, Y., WU, J. & XIAO, Z. 2021 Mechanism and modelling of the secondary baroclinic vorticity in the Richtmyer–Meshkov instability. *J. Fluid Mech.* **911**, A56.

PENNEY, W.G. & PRICE, A.T. 1945 On the changing form of a nearly spherical submarine bubble. In *Underwater Explosion Research, A Compendium of British and American Reports (Office of Naval Research, Department of the Navy)* vol. 2, pp. 145–161.

PLESSET, M.S. 1954 On the stability of fluid flows with spherical symmetry. *J. Appl. Phys.* **25**, 96–98.

RANJAN, D., NIEDERHAUS, J., MOTL, B., ANDERSON, M., OAKLEY, J. & BONAZZA, R. 2007 Experimental investigation of primary and secondary features in High-Mach-Number Shock-Bubble interaction. *Phys. Rev. Lett.* **98**, 024502.

RANJAN, D., NIEDERHAUS, J.H.J., OAKLEY, J.G., ANDERSON, M.H., BONAZZA, R. & GREENOUGH, J. 2008 Shock-bubble interactions: features of divergent shock-refraction geometry observed in experiments and simulations. *Phys. Fluids* **20**, 036101.

RANJAN, D., OAKLEY, J. & BONAZZA, R. 2011 Shock-bubble interactions. *Annu. Rev. Fluid Mech.* **43**, 117–140.

RAYLEIGH, LORD 1883 Investigation of the character of the equilibrium of an incompressible heavy fluid of variable density. *Proc. Lond. Math. Soc.* **14**, 170–177.

REESE, D.T., AMES, A.M., NOBLE, C.D., OAKLEY, J.G. & BONAZZA, R. 2018 Simultaneous direct measurements of concentration and velocity in the Richtmyer–Meshkov instability. *J. Fluid Mech.* **849**, 541–575.

RIBEYRE, X., TIKHONCHUK, V.T. & BOUQUET, S. 2004 Compressible Rayleigh–Taylor instabilities in supernova remnants. *Phys. Fluids* **16**, 4661–4670.

RICHTMYER, R.D. 1960 Taylor instability in shock acceleration of compressible fluids. *Commun. Pure Appl. Maths* **13**, 297–319.

SCHILLING, O. & LATINI, M. 2010 High-order WENO simulations of three-dimensional reshocked Richtmyer–Meshkov instability to late times: dynamics, dependence on initial conditions, and comparisons to experimental data. *Acta Math. Sci.* **30B**, 595–620.

SEWELL, E.G., FERGUSON, K.J., KRIVETS, V.V. & JACOBS, J.W. 2021 Time-resolved particle image velocimetry measurements of the turbulent Richtmyer–Meshkov instability. *J. Fluid Mech.* **917**, A41.

SI, T., LONG, T., ZHAI, Z. & LUO, X. 2015 Experimental investigation of cylindrical converging shock waves interacting with a polygonal heavy gas cylinder. *J. Fluid Mech.* **784**, 225–251.

SUN, R., DING, J., ZHAI, Z., SI, T. & LUO, X. 2020 Convergent Richtmyer–Meshkov instability of heavy gas layer with perturbed inner surface. *J. Fluid Mech.* **902**, A3.

TAYLOR, G. 1950 The instability of liquid surfaces when accelerated in a direction perpendicular to their planes. I. *Proc. R. Soc. Lond.* A **201**, 192–196.

VANDENBOOMGAERDE, M., ROUZIER, P., SOUFFLAND, D., BIAMINO, L., JOURDAN, G., HOUAS, L. & MARIANI, C. 2018 Nonlinear growth of the converging Richtmyer–Meshkov instability in a conventional shock tube. *Phys. Rev. Fluids* **3**, 014001.

WHITHAM, G.B. 1958 On the propagation of shock waves through regions of non-uniform area or flow. *J. Fluid Mech.* **4**, 337–360.

WONGA, M.L. & LELEA, S.K. 2017 High-order localized dissipation weighted compact nonlinear scheme for shock-and interface-capturing in compressible flows. *J. Comput. Phys.* **339**, 179–209.

ZHAI, Z., LIU, C., QIN, F., YANG, J. & LUO, X. 2010 Generation of cylindrical converging shock waves based on shock dynamics theory. *Phys. Fluids* **22**, 041701.

ZHAN, D., LI, Z., YANG, J., ZHU, Y. & YANG, J. 2018 Note: a contraction channel design for planar shock wave enhancement. *Rev. Sci. Instrum.* **89**, 056104.

ZHANG, Q. & GUO, W. 2016 Universality of finger growth in two-dimensional Rayleigh–Taylor and Richtmyer–Meshkov instabilities with all density ratios. *J. Fluid Mech.* **786**, 47–61.

ZHANG, Q. & SOHN, S.I. 1997 Nonlinear theory of unstable fluid mixing driven by shock wave. *Phys. Fluids* **9**, 1106–1124.

ZHOU, Y. 2017 Rayleigh–Taylor and Richtmyer–Meshkov instability induced flow, turbulence, and mixing. I. *Phys. Rep.* **720–722**, 1–136.